



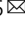


# Efficient and stable tin perovskite solar cells enabled by amorphous-polycrystalline structure

Xiao Liu<sup>1,2,6</sup>, Yanbo Wang<sup>1,6</sup>, Tianhao Wu<sup>1</sup> , Xin He<sup>2</sup>, Xiangyue Meng<sup>2</sup>, Julien Barbaud<sup>1</sup>, Han Chen<sup>1</sup>, Hiroshi Segawa<sup>3</sup>, Xudong Yang<sup>1</sup>   & Liyuan Han<sup>1</sup>  

Tin perovskite solar cells (TPSCs) have triggered intensive research as a promising candidate for lead-free perovskite solar cells. However, it is still challenging to obtain efficient and stable TPSCs because of the low defects formation energy and the oxidation of bivalent tin; Here, we report a TPSC with a stable amorphous-polycrystalline structure, which is composed of a tin triple-halide amorphous layer and cesium-formamidinium tin iodide polycrystals. This structure effectively blocks the outside oxygen, moisture and also suppresses the ion diffusion inside the devices. In addition, its energy level benefits the charge extraction and transport in TPSCs. This design enabled us to obtain the certified quasi-steady-state efficiency over 10% for TPSCs from an accredited certification institute. The cell was stable, maintaining 95% of the initial PCE after operation at the maximum power point under AM 1.5 G simulated solar light ( $100 \text{ mWcm}^{-2}$ ) for 1000 hours.

<sup>1</sup>State Key Laboratory of Metal Matrix Composites, Shanghai Jiao Tong University, 800 Dong Chuan Road, Shanghai 200240, China. <sup>2</sup>Photovoltaic Materials Group, Center for Green Research on Energy and Environmental Materials, National Institute for Materials Science, Tsukuba, Ibaraki 305-0047, Japan. <sup>3</sup>Research Center for Advanced Science and Technology, University of Tokyo, Tokyo 153-8904, Japan. <sup>4</sup>School of Materials Science and Engineering, Henan Institute of Advanced Technology, Zhengzhou University, Zhengzhou 450001, China. <sup>5</sup>Faculty of Pure and Applied Science, University of Tsukuba, Tsukuba, Ibaraki 305-8571, Japan. <sup>6</sup>These authors contributed equally: Xiao Liu, Yanbo Wang. ✉email: [Yang.xudong@sjtu.edu.cn](mailto:Yang.xudong@sjtu.edu.cn); [Han.liyuan@sjtu.edu.cn](mailto:Han.liyuan@sjtu.edu.cn)

Organic–inorganic lead halide perovskite solar cells (PSCs) have achieved great progress in the conversion of solar light into electricity at low-cost<sup>1–6</sup>. This photovoltaic technology still suffers from the potential danger of lead toxicity, which casts a shadow on its future industrialization<sup>7,8</sup>. Recently, environmental friendly tin perovskite solar cells (TPSCs) have emerged as a promising candidate for the lead-free PSCs<sup>9–15</sup>. However, it is difficult to obtain efficient and stable TPSCs because of the low defects formation energy and oxidation from Sn<sup>2+</sup> to Sn<sup>4+</sup> during the crystallization of tin perovskites<sup>16,17</sup>.

Efforts have been made to enhance the efficiency and stability, such as the application of 2D–3D hierarchy structure<sup>18–20</sup>, anti-oxidants<sup>21–24</sup>, and reducing agents<sup>25,26</sup>. In addition, mixed-cation engineering has been proved to stabilize the perovskite phase<sup>27,28</sup>. Currently, the authoritative stabilized certification of the TPSCs performance is still missing, since the cells sent to accredited institutes are required to reach a steady output and undergo repeated current–voltage (*I*–*V*) tests until the values collected under operational conditions are stable over time. The lack of stabilized certified results leaves an open question on deviations in evaluation of TPSCs. Therefore, it is highly desired to overcome the limitation on the efficiency and stability for the future application of TPSCs.

Here, we fabricate efficient and stable TPSC based on an amorphous–polycrystalline structure composed of a tin triple-halide amorphous layer and CsFASnI<sub>3</sub> polycrystals. This structure demonstrates its blocking effect on the outside moisture, oxygen, and the ion diffusion inside the devices. As a result, we achieve the certified quasi-steady-state efficiency over 10% (10.08%; Newport Laboratory, USA) for TPSCs, which retained over 95% of its initial PCE after working at the maximum power point under simulated sunlight of AM 1.5 G (100 mW cm<sup>−2</sup>) for 1000 h.

## Results

**Crystallization of tin perovskites.** Three tin perovskite films were fabricated and denoted as Sn-1X (CsFASnI<sub>3</sub>; with I<sup>−</sup> only), Sn-2X (CsFASnI<sub>3</sub>–10 mol% SnF<sub>2</sub>; F<sup>−</sup> and I<sup>−</sup>), and Sn-3X (CsFASnI<sub>3</sub>–10 mol% SnF<sub>2</sub>–20 mol% SnCl<sub>2</sub>; F<sup>−</sup>, Cl<sup>−</sup>, and I<sup>−</sup>), respectively. One thing that needed to be claimed is that EDAl<sub>2</sub> was added to all the samples (Sn-1X, Sn-2X, and Sn-3X) with the same molar ratio of 1%. It was found that EDAl<sub>2</sub> has the effects of curing pinhole and passivating surface defects in tin perovskites, as pointed at previous work<sup>13</sup>. In this case, we usually use EDAl<sub>2</sub> as an additive during the fabrication of tin perovskite films. Since all the samples here were added EDAl<sub>2</sub> with the same concentration, we could exclude the effects of EDAl<sub>2</sub> on the differences between Sn-1X, Sn-2X, and Sn-3X, as are shown below. Figure 1a–c show the scanning electron microscopy (SEM) images of the three samples. Obviously, Sn-1X film showed poor crystallization with large gaps between grains (Fig. 1a), which can notoriously deteriorate the separation and collection of photo-generated charge carriers. In contrast, the morphology of Sn-2X film was improved but pin-holes appeared with white dots on the surface (Fig. 1b), which could be ascribed to the phase segregation induced by SnF<sub>2</sub> according to previous reports<sup>29,30</sup>. When the amount of SnF<sub>2</sub> was further increased to 20 mol% in Sn-2X film, the number of pin-holes reduced but more white dots were observed (Supplementary Fig. 1a). The white dots would increase the surface roughness and the pin-holes can lead to the deterioration of TPSCs. For the Sn-3X perovskite film, a pin-hole free and dense layer with a large grain size of 600–1000 nm was obtained (Fig. 1c). We also fabricated Sn-3X films with different amount of SnCl<sub>2</sub>. Pin-holes still remained in the sample of Sn-3X film with 10 mol% SnCl<sub>2</sub> while for the Sn-3X film with 30 mol%

SnCl<sub>2</sub>, non-uniform thick-layered structure could be observed (Supplementary Fig. 1b, c). The corresponding XRD patterns for these Sn-3X films were also provided in Supplementary Fig. 2. To verify whether it will also work without SnF<sub>2</sub>, we fabricated the tin perovskites using only SnCl<sub>2</sub> as the additive. However, the crystallization was found to be poor with lots of pin-holes (Supplementary Fig. 1d–f). One thing that concerned us is that, different from the morphology of Sn-2X film, layered structure seemed to be formed on the surface of Sn-3X film, which will be discussed in the next section.

The X-ray diffraction (XRD) pattern indicates that Sn-1X, Sn-2X, and Sn-3X films are all crystallized with a similar orthorhombic structure as CsFASnI<sub>3</sub> (Fig. 1d)<sup>9,31</sup>, but the Sn-3X shows a remarkably stronger peak intensity corresponding to the (100) and (200) face than the other two samples. This proves that Sn-3X was well crystallized with high-preferred orientation in  $\langle X00 \rangle$  direction. The photoluminescence (PL) and time-resolved photoluminescence decay (TRPL) measurements of the corresponding three samples are shown in Supplementary Figs. 3 and 4. The highest PL signal as well as the longest carrier lifetime for Sn-3X film indicated the lowest non-radiative recombination among all three perovskite film, which would be benefit for the enhancement of  $V_{oc}$ <sup>13,32,33</sup>.

**Characterizations of amorphous layer.** In order to further investigate the structure of Sn-3X perovskite film, grazing incident X-ray diffraction (GIXRD) was performed (Fig. 1e). Compared to the XRD pattern of Sn-3X (Fig. 1d, blue line), no new patterns appeared with the incident angles changing from 0.5° to 0.1°, which indicates no new crystal structure was formed for Sn-3X. We then conducted the transmission electron microscopy (TEM). The sample was prepared by focused ion beam technique and protective layer of Au was deposited before ion-beam etching to exclude the effect of the environment. As can be seen in Fig. 1f, a well-crystallized Sn-3X film was covered by an amorphous layer with the thickness of 3–4 nm on it. To make it clearer, the magnified high-resolution TEM (HRTEM) image (Fig. 1f; right top) was given. Combined with the results from GIXRD and TEM, we reasoned that an amorphous layer was assembled on the surface of Sn-3X perovskite to form an amorphous–polycrystalline structure. The band gaps of Sn-3X with different content of Cl were measured by UV–visible absorption spectroscopy (Supplementary Fig. 5a–c) and the results were transformed using the Kubelka–Munk equation (Supplementary Fig. 5d–f). There is no obvious change in bandgaps of Sn-3X films (Supplementary Fig. 6), which confirms the structure of perovskite crystals was maintained when the amorphous layer was formed at the surface.

X-ray photoelectron spectroscopy (XPS) survey spectra were obtained to find out the composition of the amorphous layer (Supplementary Fig. 7a, b). According to the XPS results, the ratios of I:Sn are 1:0.58 and 1:1.47 for Sn-2X and Sn-3X, respectively, as listed in Supplementary Fig. 7c, which means a lower content of iodide was left on the Sn-3X perovskite surface. Moreover, for Sn-3X film, the atomic ratios of I:Cl and I:F were 1:0.44 and 1:0.29 (Supplementary Fig. 7d), respectively, which were much lower than 1:0.132 of I:Cl and 1:0.066 of I:F in the precursor solution of Sn-3X film. The Cl and F content at the Sn-3X perovskite surface is higher than that in precursor solution, which proves that the amorphous layer is composed of the tin triple halide of F, Cl, and I, not only a layer of SnCl<sub>2</sub>. As we all know, SnCl<sub>2</sub> is even more hygroscopic than perovskites themselves, which will deteriorate the stability of the devices. However, the contact angle with water is enlarged from 58.9° to 89° under the existence of the amorphous layer (Supplementary

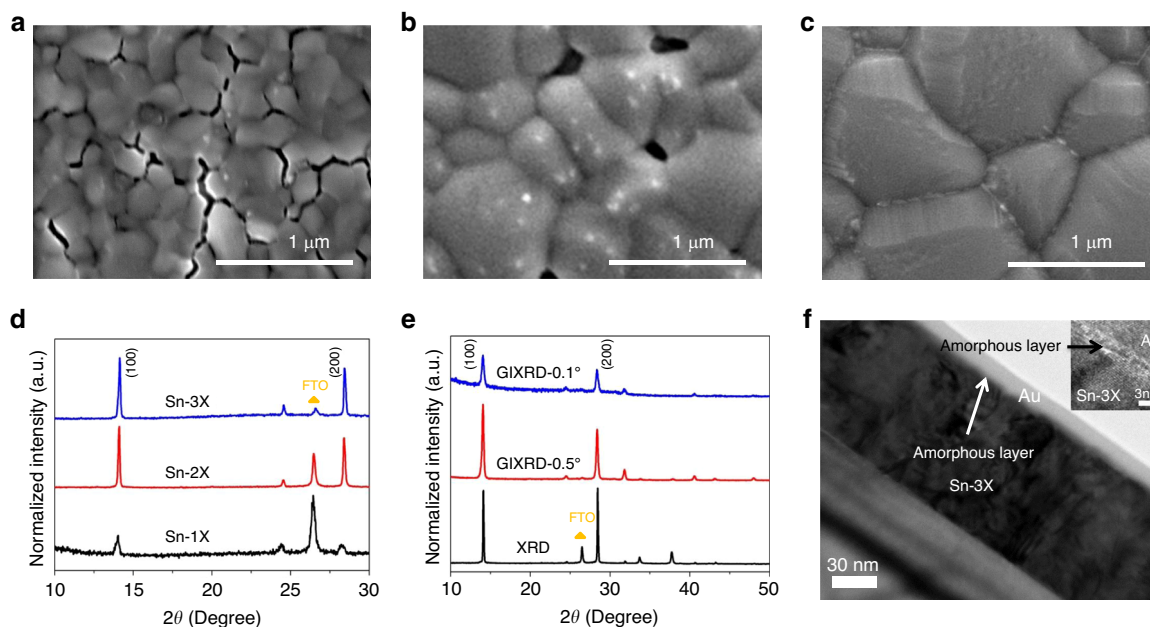


**Fig. 1 Crystallization of tin perovskite films.** **a** SEM images of Sn-1X, **b** Sn-2X, and **c** Sn-3X. **d** The XRD patterns of the corresponding three samples. **e** The XRD and GIXRD patterns of Sn-3X; the incident angles of GIXRD are 0.5° and 0.1°, respectively. **f** TEM and HRTEM (inset) images of Sn-3X film sample fabricated by focused ion beam technique.

Fig. 10a–c (top)), which further confirmed that it is not simply a layer of  $\text{SnCl}_2$ . In addition, we performed the measurement of time-of-flight secondary ion mass spectroscopy (ToF-SIMS) for the Sn-3X sample to show the depth profile for the elements (Supplementary Fig. 8a). It was found that the elements of F, Cl concentrated at the surface of Sn-3X whereas I was homogeneously distributed across the film. The F and Cl quickly dropped after 8 s of sputtering time, which is consistent with the XPS results and further confirmed that the amorphous layer only existed at the surface. The element of Cl at the  $x$ - $y$  plane (Supplementary Fig. 8b) showed uniform distribution, indicating a high coverage ratio of this amorphous layer on the surface of Sn-3X films. Otherwise, bright signals of Cl would be found.

In order to check the surface of the Sn-1X and Sn-2X films, TEM tests were also performed for the Sn-1X and Sn-2X samples (Supplementary Fig. 9); no such amorphous layer was found. The reason for the formation of the amorphous-polycrystalline structure may be the low surface energy of this amorphous layer<sup>34,35</sup>. The contact angles of water and toluene on the surface of Sn-1X, Sn-2X, and Sn-3X with different contents of  $\text{SnCl}_2$  samples were measured (Supplementary Fig. 10), and the corresponding surface energies were estimated using the Owens–Wendt model<sup>36</sup>. After calculation, we found that the surface energy was sharply reduced from 46.3 to 30.6  $\text{mJ m}^{-2}$  from Sn-1X to Sn-3X samples. In addition, according to Supplementary Fig. 11a, b and the calculated surface energy values shown in Supplementary Table 1, we found that the surface energy could be further changed as the Cl content varied in Sn-3X samples, but the amount of  $\text{SnF}_2$  did not have this effect (Supplementary Fig. 11a, c and Table 1). Therefore, the formation of the amorphous-polycrystalline structure can be simply controlled by the amount of  $\text{SnCl}_2$ .

**Stability of the amorphous-polycrystalline structure.** The XRD patterns as a function of time were monitored to test the degradation of Sn-2X and Sn-3X films without encapsulation in ambient conditions with the humidity around 60% and temperature of 25 °C. As shown in Supplementary Fig. 12a, the aged

Sn-2X film was found to show a much lower peak at 14.1° and 28.4° compared to the feature signal of fluorine-doped tin oxide substrate (FTO) at 26.5° than the fresh sample. In contrast, the feature signals of Sn-3X sample maintained the ratio to the signals of FTO (Supplementary Fig. 12b). We carefully compared the deterioration in the intensity of (100) peaks; the decay rate of Sn-2X turned out to be much faster than that of the Sn-3X sample (Fig. 2c, d), which proved the better stability of the amorphous-polycrystalline structure in Sn-3X film to oxygen and moisture. The improved stability could be attributed to the larger water contact angle of the tin triple-halide amorphous layer compared to that of Sn-2X films (Supplementary Fig. 10b, c) and its blocking of oxygen. The larger crystalline grains in Sn-3X films with fewer defects also reduced the channels for oxygen and water intrusion.

The light soaking stability of Sn-2X and Sn-3X films in  $\text{N}_2$  environment was also compared. XPS for Sn-2X and Sn-3X films were performed before and after aging test under AM 1.5 G simulated solar light ( $100 \text{ mW cm}^{-2}$ ) (Fig. 2a, b). For the fresh samples, it was observed that the width of the Sn 3d core level in Sn-3X film was larger than that in Sn-2X, which could be ascribed to the formation of the amorphous layer in Sn-3X film. To further confirm our speculation, we etched the surface of Sn-3X with Ar ion beam to remove the amorphous layer and measured the XPS of inner perovskite (Supplementary Fig. 13); narrower Sn 3d signal was obtained. More importantly, the ratios of  $\text{Sn}^{2+}$  and  $\text{Sn}^{4+}$  were calculated before and after light soaking (Supplementary Fig. 14). It was found that the aged Sn-3X film had much less  $\text{Sn}^{4+}$  than Sn-2X film than the aged Sn-2X film. The stability under heat in the dark was measured by UV–visible absorption spectroscopy in  $\text{N}_2$ . After 6 h of heating at 85 °C, Sn-2X underwent fast decay in the intensity of absorption, whereas Sn-3X maintained the absorption for 100 h (Supplementary Fig. 15a, b). The absorption decay at the wavelength of 500 nm was recorded in Supplementary Fig. 16. These results indicate the Sn-3X with this amorphous-polycrystalline structure is more stable under light and heat. The reason for the enhanced light-soaking and heat stability could be attributed to the suppressed

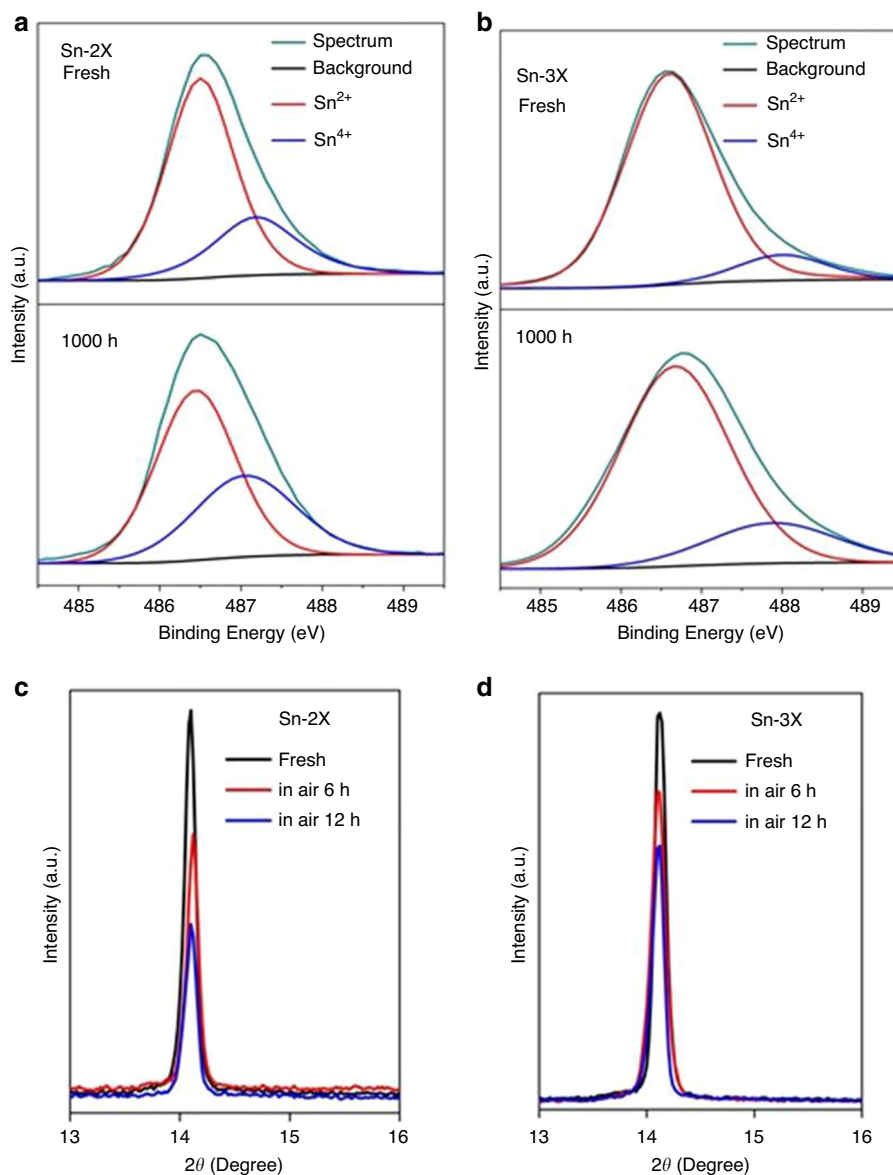


**Fig. 2** The characterization of the stability of tin perovskite layers. **a** High-resolution XPS spectrum of the Sn  $3d_{5/3}$  region of Sn-2X and **b** Sn-3X film before (top) and after (bottom) being exposed to continuous simulated sunlight AM 1.5 G ( $100 \text{ mW cm}^{-2}$ ) for 1000 h, respectively. The normalized intensity of the (100) peak in XRD patterns of **c** Sn-2X and **d** Sn-3X films as a function of time in ambient air.

ion migration. Devices with a structure of FTO/PEDOT:PSS/Perovskite/PCBM/BCP/Ag were fabricated based on Sn-2X and Sn-3X films and aged at the maximum power point under continuous light-soaking of AM 1.5 G ( $100 \text{ mW cm}^{-2}$ ) and  $85^\circ \text{C}$  for 100 h. XPS was used to detect the  $\text{I}^-$  signal in Ag electrodes (Supplementary Fig. 17); the signal of  $\text{I}^-$  in Ag electrode for the device based on Sn-2X is much higher than that in the device based on Sn-3X.

**Device performance.** We then fabricated TPSC with an inverted planar structure and the cross-section SEM image of this configuration is shown in Fig. 3a. During the fabrication process, we confirmed that the amorphous-polycrystalline structure would not affect the wetting property of PCBM solution on Sn-3X film even though the contact angle was increased from  $7.8^\circ$  to  $18^\circ$  (Supplementary Fig. 18). The  $I$ - $V$  curves of Sn-2X and Sn-3X-based cells under both scan directions are shown in Fig. 3b. The Sn-2X-based TPSC obtained an initial PCE of 6.9%, with open-circuit voltage ( $V_{\text{oc}}$ ) of 0.55 V, current density ( $J_{\text{sc}}$ ) of  $18.6 \text{ mA cm}^{-2}$ ,

and fill factor (FF) of 67.4% under forward scan. In contrast, the PCE of Sn-3X-based TPSC was 10.4% with a  $V_{\text{oc}}$  of 0.64 V, a  $J_{\text{sc}}$  of  $21.6 \text{ mA cm}^{-2}$ , and FF of 75.2%. The detailed device parameters are summarized in Supplementary Table 2. The integrated current density of 18.7 and  $21.8 \text{ mA cm}^{-2}$  for Sn-2X-based and Sn-3X-based devices calculated from the monochromatic incident photo-to-current conversion efficiency (IPCE) (Fig. 3c) matched well with the  $I$ - $V$  test. The  $I$ - $V$  curves of the devices based on Sn-3X films with different amount of  $\text{SnCl}_2$  or the devices using only  $\text{SnCl}_2$  as the additives are also shown, respectively, in Supplementary Figs. 19 and 20. The improvement in device performance for Sn-3X-based devices was generally consistent across 16 devices according to the statistical box chart (Fig. 3d). To further investigate the reasons for this improvement, the band gap of this amorphous layer was measured to be 1.67 eV via electron energy loss spectroscopy (Supplementary Fig. 21). In addition, its valence band maximum (VBM) of  $-5.5 \text{ eV}$  was also given by photoelectron spectroscopy (Supplementary Fig. 22b). Combined with the band gap of Sn-3X perovskite measured in Supplementary

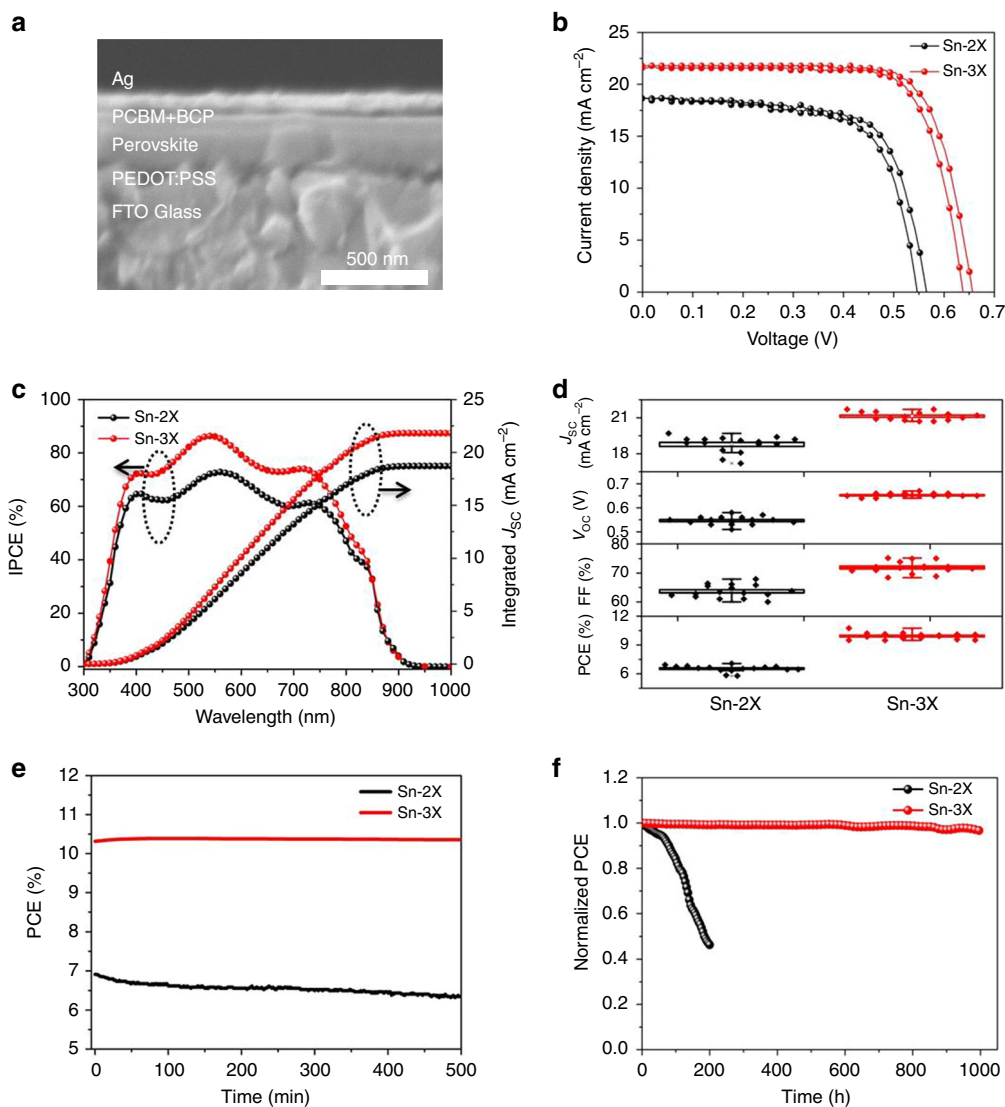


**Fig. 3** Configuration and device performance of TPSCs. **a** Cross-section SEM image of the cell based on amorphous-polycrystalline structure. **b** The  $I$ - $V$  curves of Sn-2X and Sn-3X-based TPSCs. **c** The IPCE of the corresponding devices. **d** The statistical box chart of the parameters of corresponding devices and 16 cells were fabricated for each type. **e** The stabilized output of the corresponding devices for 500 min. **f** The stability test under simulated AM 1.5 G ( $100 \text{ mW cm}^{-2}$ ) at the maximum power point. All the cells were encapsulated in  $\text{N}_2$  gas environment.

Fig. 5f and the VBM measured in Supplementary Fig. 22c, the energy level alignment of the whole device is summarized in Supplementary Fig. 23. The appropriate conduction band minimum of this amorphous layer right between those of Sn-3X perovskite and PCBM could induce less charge recombination and energy loss in devices. Dark current and transient photocurrent and photovoltage were measured to demonstrate the charge recombination and transport in a full device. As is shown in Supplementary Fig. 24, the dark current of Sn-3X-based device was three times lower than that of Sn-2X-based device. Meanwhile, the transient photovoltage results of Sn-3X-based device showed a longer decay time of  $63.5 \mu\text{s}$  than the value  $16.8 \mu\text{s}$  for the Sn-2X-based device (Supplementary Fig. 25a). Both dark current and transient photovoltage measurement demonstrated a lower charge recombination in a Sn-3X-based device<sup>37,38</sup>. In addition, Sn-3X-based cells showed faster decay in transient photocurrent with a lifetime of  $1.37 \mu\text{s}$  compared to the  $3.45 \mu\text{s}$  of the Sn-2X-based cell (Supplementary Fig. 25b), indicating better charge transport in Sn-3X-based devices<sup>39,40</sup>. The corresponding stabilized power output of Sn-2X and Sn-3X are shown in Fig. 3e,

where Sn-3X presented a constant stabilized output efficiency of about 10.3% with an applied voltage of 0.52 V for 500 min. In contrast, Sn-2X-based cell tended to exhibit a slow decrease in stabilized output during the whole test. Furthermore, the Sn-3X cells encapsulated in a  $\text{N}_2$  glove box maintained over 95% of its initial PCE after operation at the maximum power point under simulated illumination of AM 1.5 G ( $100 \text{ mW cm}^{-2}$ ) for 1000 h. In contrast, Sn-2X-based cell lost more than 50% of PCE within 200 h (Fig. 3f). One of our typical Sn-3X-based cells was sent to an accredited test center (Newport, USA); a certified efficiency of 10.08% was obtained with a  $V_{oc}$  of 0.64 V,  $J_{sc}$  of  $22.2 \text{ mA cm}^{-2}$  and FF of 70.8% (Supplementary Fig. 26). The certified results of  $I$ - $V$  curve (Supplementary Fig. 27) and normalized external quantum efficiency (EQE) (Supplementary Fig. 28) were also provided. More importantly, it should be noted that the certified efficiency obtained here is a quasi-steady-state efficiency, which means that every point in the  $I$ - $V$  curve will not be obtained until the current can be unchanging at a level within 0.03% under a constant applied voltage, indicating the reliable working stability of TPSC based on this amorphous-polycrystalline structure.

## Discussion

In this work, we fabricated a TPSC with an amorphous-polycrystalline structure, which enabled high efficiency and stable TPSCs due to its suitable energy level and blocking effect on ion diffusion, oxygen, and moisture. The certified quasi-steady-state efficiency over 10% for TPSCs was achieved from an accredited center. Our work indicates a way to build efficient and stable TPSCs with reliable measurement results.

## Methods

**Materials.** The following chemicals were used as received from commercial sources, including SnI<sub>2</sub> (99.99%, Sigma-Aldrich), CsI (99.9%, Sigma-Aldrich), CH(NH<sub>2</sub>)<sub>2</sub>I (FAI) (>98%, Tokyo Chemical Industry Co., Japan), SnF<sub>2</sub> (>99%, Sigma-Aldrich), SnCl<sub>2</sub> (>99%, Sigma-Aldrich), PCBM (99.5% Lumtec Co., Taiwan), bathocuproine (>99%, Wako), ethylenediammonium diiodide (EDAI<sub>2</sub>) (>98%, Tokyo Chemical Industry Co., Japan). All solutions were filtered with 0.2 μm PTFE filter before use.

**Solar cell fabrication.** FTO glass substrates were patterned and cleaned by detergent, DI water, acetone, and isopropanol for 20 min via sonication treatment, respectively. Then, the substrates were treated by ultraviolet-ozone for 30 min before the deposition of PEDOT:PSS. For CsFASnI<sub>3</sub> perovskite precursor solution, CsI, FAI, SnI<sub>2</sub>, SnF<sub>2</sub>, EDAI<sub>2</sub> with a molar ratio of 0.2:0.8:1:0.1:0.01 were dissolved in DMSO solvent with a total concentration of 0.9 M<sup>13,33,41</sup>. Different concentrations of SnCl<sub>2</sub> were added to the CsFASnI<sub>3</sub> precursor solution to study their effect. (The molar ratio of cesium was fixed to 20 mol% according to previous work.)<sup>42</sup> The perovskite films were spin-coated on the PEDOT:PSS layer at 1000 rpm for 12 s, and 5000 rpm for 40 s in the glove box. 150 μl of chlorobenzene was in-situ dripped onto the perovskite film after 30 s during the second step. Afterward, the perovskite films were annealed at 60 °C for 5 s and 100 °C for 15 min. PCBM (20 mg/ml in chlorobenzene) solution was spin-coated onto the perovskite film at 1000 rpm for 60 s and 5000 rpm for 5 s. Finally, 8 nm BCP and 100 nm Ag electrode were evaporated under high vacuum (<2 × 10<sup>-7</sup> Torr). The device area was defined using masks as 0.09 cm<sup>2</sup>, respectively. The devices were fabricated in a glove box filled with N<sub>2</sub> and the oxygen concentration was always kept under 0.1 ppm. Finally, the solar cells were encapsulated in N<sub>2</sub>-filled glove box by cavity glass with UV glue on the edges. The encapsulation was finished after 10 s of soaking under UV light and the photographs of our encapsulated device are provided in Supplementary Fig. 29. The solar cells sent to the certification institute were further packaged in a black cooling system to keep the temperature around 25 °C.

**Characterization.** The SEM images were measured by JSM-6500F field-emission scanning electron microscope. The XRD was measured by Rigaku RINT-2500 powder X-ray diffractometer using Cu K<sub>α</sub> radiation. The transmission electron microscope (TEM), high-resolution transmission electron microscope (HRTEM), and electron energy loss spectroscopy were obtained by a JEM-2100F field emission electron microscope. To prepare TEM sample by focused ion beam (JEM-9320FIB), the protective layers of Au were deposited before ion-beam etching. To prepare other TEM samples, the perovskite films were removed from FTO glass to Cu grid in a nitrogen-filled glovebox and transformed to TEM chamber with the protection of N<sub>2</sub> gas to prevent the possible oxidation of the film. The UV-vis spectra were obtained by a Shimadzu UV/vis 3600 spectrophotometer. The photoelectron spectroscopies were measured by a photoelectron spectrometer (Riken-keiki AC-3). The PL and TRPL decay were measured with a Hamamatsu fluorescence spectrometer. The XPS spectra were measured by PHI Quantera SXM (ULVAC-PHI) with X-ray source of Al K<sub>α</sub> (mono), the incident angle and take off angle are 90° and 45°, respectively. Surface energy was estimated using the Owens-Wendt model<sup>36</sup>, the equations are as follows:

$$r_s = r_s^D + r_s^P \quad (1)$$

$$r_L = r_L^D + r_L^P \quad (2)$$

$$r_L(1 + \cos \theta) = 2(r_s^D r_L^D)^{1/2} + 2(r_s^P r_L^P)^{1/2} \quad (3)$$

In Eq. (1),  $r_s$  is the overall surface energy of the solid,  $r_s^D$  is the dispersive component of the surface tension of the solid,  $r_s^P$  is the polar component of the surface tension of the solid. In Eq. (2),  $r_L$  is the overall surface tension of the wetting liquid,  $r_L^D$  is the dispersive component of the surface tension of the wetting liquid,  $r_L^P$  is the polar component of the wetting liquid. In Eq. (3),  $\theta$  is the contact angle of liquid on a solid surface. Water ( $r_L^D = 21.8 \text{ mJ m}^{-2}$ ,  $r_L^P = 51.0 \text{ mJ m}^{-2}$ ) and Toluene ( $r_L^D = 28.4 \text{ mJ m}^{-2}$ ,  $r_L^P = 0 \text{ mJ m}^{-2}$ ) were used as tested liquid. The  $J$ - $V$  curves were measured under forward scan (−0.1 to 0.7 V) or reverse scan (0.7 to −0.1 V) with a fixed step voltage of 10 mV and delay time of 50 ms by a solar simulator with standard air mass 1.5 sunlight (100 mW cm<sup>-2</sup>, WXS-155S-10, Wacom Denso) in air at room temperature near 25 °C according to our previous report<sup>43,44</sup>. We used a reference cell, which was calibrated by the Calibration,

Standards and Measurement Team at the Research Center for Photovoltaics in AIST, Japan. The spectral mismatch is <3%. The aperture area was defined by a mask of 0.09 cm<sup>2</sup>. Monochromatic IPCE spectra were measured by a monochromatic incident light of 1 × 10<sup>16</sup> photons cm<sup>-2</sup> in director current mode (CEP-2000BX, Bunko-Keiki). The light intensity of the solar simulator was calibrated by a standard silicon solar cell. The operational stability was tested on a solar cell light resistance test system (Model BIR-50, Bunko-keiki) with a Class AAA solar simulator. Then the operational stability was tested on a solar cell light resistance test system (Model BIR-50, Bunko-keiki) with a Class AAA solar simulator. All the tests except for the stability test in ambient air are using the encapsulated cells or the samples kept in boxes filled with N<sub>2</sub>, and transferred using those boxes too to exclude the formation of Sn-oxide<sup>45</sup>. The cells used for the ToF-SIMS tests are encapsulated first to undergo the aging test and then were unpackaged to test the ToF-SIMS.

**Reporting summary.** Further information on research design is available in the Nature Research Reporting Summary linked to this article.

## Data availability

The data that support the findings of this study are available from the corresponding authors on reasonable request.

Received: 7 February 2020; Accepted: 6 May 2020;

Published online: 29 May 2020

## References

- Kojima, A., Teshima, K., Shirai, Y. & Miyasaka, T. Organometal halide perovskites as visible-light sensitizers for photovoltaic cells. *J. Am. Chem. Soc.* **131**, 6050–6051 (2009).
- Kim, H. S. et al. Lead iodide perovskite sensitized all-solid-state submicron thin film mesoscopic solar cell with efficiency exceeding 9%. *Sci. Rep.* **2**, 591 (2012).
- Yang, W. S. et al. Iodide management in formamidinium-lead-halide-based perovskite layers for efficient solar cells. *Science* **356**, 1376–1379 (2017).
- Jiang, Q. et al. Surface passivation of perovskite film for efficient solar cells. *Nat. Photonics* **13**, 460–466 (2019).
- Jung, E. H. et al. Efficient, stable and scalable perovskite solar cells using poly(3-hexylthiophene). *Nature* **567**, 511–515 (2019).
- Wang, Y. et al. Stabilizing heterostructures of soft perovskite semiconductors. *Science* **365**, 687–691 (2019).
- Flora, G., Gupta, D. & Tiwari, A. Toxicity of lead: a review with recent updates. *Interdiscip. Toxicol.* **5**, 47–58 (2012).
- Ke, W. & Kanatzidis, M. G. Prospects for low-toxicity lead-free perovskite solar cells. *Nat. Commun.* **10**, 965 (2019).
- Stoumpos, C. C., Malliakas, C. D. & Kanatzidis, M. G. Semiconducting tin and lead iodide perovskites with organic cations: phase transitions, high mobilities, and near-infrared photoluminescent properties. *Inorg. Chem.* **52**, 9019–9038 (2013).
- Hao, F., Stoumpos, C. C., Cao, D. H., Chang, R. P. H. & Kanatzidis, M. G. Lead-free solid-state organic-inorganic halide perovskite solar cells. *Nat. Photonics* **8**, 489–494 (2014).
- Noel, N. K. et al. Lead-free organic-inorganic tin halide perovskites for photovoltaic applications. *Energy Environ. Sci.* **7**, 3061–3068 (2014).
- Lee, S. J. et al. Fabrication of efficient formamidinium tin iodide perovskite solar cells through SnF<sub>2</sub>-pyrazine complex. *J. Am. Chem. Soc.* **138**, 3974–3977 (2016).
- Jokar, E. et al. Slow surface passivation and crystal relaxation with additives to improve device performance and durability for tin-based perovskite solar cells. *Energy Environ. Sci.* **11**, 2353–2362 (2018).
- Jiang, X. et al. Ultra-high open-circuit voltage of tin perovskite solar cells via an electron transporting layer design. *Nat. Commun.* **11**, 1245 (2020).
- Meng, X. et al. Surface-controlled oriented growth of FASnI<sub>3</sub> crystals for efficient lead-free perovskite solar cells. *Joule* **4**, 902–912 (2020).
- Noel, N. K. et al. Lead-free organic-inorganic tin halide perovskites for photovoltaic applications. *Energy Environ. Sci.* **7**, 3061–3068 (2014).
- Koh, T. M. et al. Formamidinium tin-based perovskite with low Eg for photovoltaic applications. *J. Mater. Chem. A* **3**, 14996–15000 (2015).
- Liao, Y. Q. et al. Highly oriented low-dimensional tin halide perovskites with enhanced stability and photovoltaic performance. *J. Am. Chem. Soc.* **139**, 6693–6699 (2017).
- Shao, S. Y. et al. Highly reproducible Sn-based hybrid perovskite solar cells with 9% efficiency. *Adv. Energy Mater.* **8**, 1702019 (2018).
- Wang, F. et al. 2D-Quasi-2D-3D hierarchy structure for tin perovskite solar cells with enhanced efficiency and stability. *Joule* **2**, 2732–2743 (2018).

21. Kumar, M. H. et al. Lead-free halide perovskite solar cells with high photocurrents realized through vacancy modulation. *Adv. Mater.* **26**, 7122–7127 (2014).
22. Kayesh, M. E. et al. Enhanced photovoltaic performance of FASnI<sub>3</sub>-based perovskite solar cells with hydrazinium chloride coadditive. *ACS Energy Lett.* **3**, 1584–1589 (2018).
23. Tai, Q. et al. Antioxidant grain passivation for air-stable tin-based perovskite solar cells. *Angew. Chem. Int. Ed.* **58**, 806–810 (2019).
24. Marshall, K. et al. Enhanced stability and efficiency in hole-transport-layer-free CsSnI<sub>3</sub> perovskite photovoltaics. *Nat. Energy* **1**, 16178 (2016).
25. Song, T. B. et al. Importance of reducing vapor atmosphere in the fabrication of tin-based perovskite solar cells. *J. Am. Chem. Soc.* **139**, 836–842 (2017).
26. Gu, F. et al. Improving performance of lead-free formamidinium tin triiodide perovskite solar cells by tin source purification. *Sol. RRL* **2**, 1800136 (2018).
27. Gao, W. et al. Robust stability of efficient lead-free formamidinium tin iodide perovskite solar cells realized by structural regulation. *J. Phys. Chem. Lett.* **9**, 6999–7006 (2018).
28. Prasanna, R. et al. Band gap tuning via lattice contraction and octahedral tilting in perovskite materials for photovoltaics. *J. Am. Chem. Soc.* **139**, 11117–11124 (2017).
29. Zhao, Z. et al. Mixed-organic-cation tin iodide for lead-free perovskite solar cells with an efficiency of 8.12%. *Adv. Sci.* **4**, 1700204 (2017).
30. Xu, X. et al. Ascorbic acid as an effective antioxidant additive to enhance the efficiency and stability of Pb/Sn-based binary perovskite solar cells. *Nano Energy* **34**, 392–398 (2017).
31. Wang, F. et al. Organic cation-dependent degradation mechanism of organotin halide perovskites. *Adv. Funct. Mater.* **26**, 3417–3423 (2016).
32. Kim, H. et al. Boosting the performance and stability of quasi-two-dimensional tin-based perovskite solar cells using the formamidinium thiocyanate additive. *J. Mater. Chem. A* **6**, 18173–18182 (2018).
33. Jokar, E., Chien, C.-H., Tsai, C.-M., Fathi, A. & Diau, E. W.-G. Robust tin-based perovskite solar cells with hybrid organic cations to attain efficiency approaching 10%. *Adv. Mat.* **31**, 1804835 (2019).
34. Zhao, H. et al. Enhanced stability and optoelectronic properties of MAPbI<sub>3</sub> films by a cationic surface-active agent for perovskite solar cells. *J. Mater. Chem. A* **6**, 10825 (2018).
35. Wang, S. et al. Water-soluble triazolium ionic-liquid-induced surface self-assembly to enhance the stability and efficiency of Perovskite solar cells. *Adv. Funct. Mater.* **29**, 1900417 (2019).
36. Owens, D. K. et al. Estimation of the surface free energy of polymers. *J. Appl. Polym. Sci.* **13**, 1741–1747 (1969).
37. Wu, T. et al. Efficient defect passivation for perovskite solar cells by controlling the electron density distribution of donor- $\pi$ -acceptor molecules. *Adv. Energy Mater.* **9**, 1803766 (2019).
38. Wu, T. et al. Efficient and stable CsPbI<sub>3</sub> solar cells via regulating lattice distortion with surface organic terminal groups. *Adv. Mater.* **31**, e1900605 (2019).
39. Zuo, L. J. et al. Polymer-modified halide perovskite films for efficient and stable planar heterojunction solar cells. *Sci. Adv.* **3**, e1700106 (2017).
40. Adhikari, N. et al. Crystallization of a perovskite film for higher performance solar cells by controlling water concentration in methyl ammonium iodide precursor solution. *Nanoscale* **8**, 2693–2703 (2016).
41. Ke, W. et al. Enhanced photovoltaic performance and stability with a new type of hollow 3D perovskite {en}FASnI<sub>3</sub>. *Sci. Adv.* **3**, e1701293 (2017).
42. Liu, X. et al. Improved efficiency and stability of Pb–Sn binary perovskite solar cells by Cs substitution. *J. Mater. Chem. A* **4**, 17939–17945 (2016).
43. Wang, Y. et al. Reliable measurement of perovskite solar cells. *Adv. Mater.* **31**, e1803231 (2019).
44. Yin, M. S. et al. Accurate and fast evaluation of perovskite solar cells with least hysteresis. *Appl. Phys. Express* **10**, 076601 (2017).
45. Chen, M. et al. Highly stable and efficient all-inorganic lead-free perovskite solar cells with native-oxide passivation. *Nat. Commun.* **10**, 16 (2019).

## Acknowledgements

This work was supported by the National Natural Science Foundation of China (grant numbers 11574199, 11674219, and 11834011), the New Energy and Industrial Technology Development Organization (NEDO, Japan) and the KAKEHI Grant of Japan (Grant No. 18H02078).

## Author contributions

X.L., Y.W., L.H., and X.Y. conceived the idea, X.L. and Y.W. initialized this project and carried out device fabrication and characterization. T.W. performed the TOF-SIMS measurement. T.W., X.H., X.M., J.B., H.C. and H.S. were involved in the data analysis. X.L., Y.W., L.H. and X.Y. wrote the manuscript. L.H. and X.Y. supervised the whole project. All authors discussed and reviewed final manuscript.

## Competing interests

The authors declare no competing interests.

## Additional information

**Supplementary information** is available for this paper at <https://doi.org/10.1038/s41467-020-16561-6>.

**Correspondence** and requests for materials should be addressed to X.Y. or L.H.

**Peer review information** *Nature Communications* thanks the anonymous reviewer(s) for their contribution to the peer review of this work.

**Reprints and permission information** is available at <http://www.nature.com/reprints>

**Publisher's note** Springer Nature remains neutral with regard to jurisdictional claims in published maps and institutional affiliations.



**Open Access** This article is licensed under a Creative Commons Attribution 4.0 International License, which permits use, sharing, adaptation, distribution and reproduction in any medium or format, as long as you give appropriate credit to the original author(s) and the source, provide a link to the Creative Commons license, and indicate if changes were made. The images or other third party material in this article are included in the article's Creative Commons license, unless indicated otherwise in a credit line to the material. If material is not included in the article's Creative Commons license and your intended use is not permitted by statutory regulation or exceeds the permitted use, you will need to obtain permission directly from the copyright holder. To view a copy of this license, visit <http://creativecommons.org/licenses/by/4.0/>.

© The Author(s) 2020